catalysts

MDPI

Review

Research Progress in ZIF-8 Derived Single Atomic Catalysts for Oxygen Reduction Reaction

Siqi Shen, Yuanyuan Sun, Hao Sun, Yuepeng Pang, Shuixin Xia, Taiqiang Chen, Shiyou Zheng * and Tao Yuan *

School of Materials and Chemistry, University of Shanghai for Science and Technology, Shanghai 200093, China; ssqgood4591@163.com (S.S.); 202342915@st.usst.edu.cn (Y.S.); 13816439928@163.com (H.S.); pangyp@usst.edu.cn (Y.P.); xiashuixin001@163.com (S.X.); tqchen@usst.edu.cn (T.C.)

* Correspondence: syzheng@usst.edu.cn (S.Z.); yuantao@usst.edu.cn (T.Y.)

Abstract: Transition metal (TM) single atomic catalysts (M_{SAC}-N-C) derived from doped zeolite imidazolate frameworks (ZIF-8) are considered attractive oxygen reduction reaction (ORR) catalysts for fuel cells and metal-air batteries due to their advantages of high specific surface area, more active catalytic sites, adjustable pore size, and coordination topology features. This review provides an updated overview of the latest advances of M_{SAC}-N-C catalysts derived from ZIF-8 precursors in ORR electrocatalysis. Particularly, some key challenges, including coordination environments regulation of catalysis center in M_{SAC}-N-C, the active sites loading optimization and synergistic effects between TM nanoclusters/nanoparticles and the single atoms on M_{SAC}-N-C catalysis activity, as well as their adaptability in various devices, are summarized for improving future development and application of M_{SAC}-N-C catalysts. In addition, this review puts forward future research directions, making it play a better role in ORR catalysis for fuel cells and metal air batteries.

Keywords: oxygen reduction reaction; transition metal single atomic catalyst; zeolite imidazolate framework (ZIF-8); catalytic performance

check for updates

Citation: Shen, S.; Sun, Y.; Sun, H.; Pang, Y.; Xia, S.; Chen, T.; Zheng, S.; Yuan, T. Research Progress in ZIF-8 Derived Single Atomic Catalysts for Oxygen Reduction Reaction. *Catalysts* **2022**, *12*, 525. https://doi.org/10.3390/catal12050525

Academic Editors: Chao Su and Junling Lu

Received: 7 March 2022
Accepted: 4 May 2022
Published: 7 May 2022

1. Introduction

With the ever-increasing issues of environmental pollution and shortage of fossil energy, renewable energy generation and storage systems with high efficiency, cleanliness and low cost are especially needed. Among all the new energy generation systems, fuel cells (especially H_2-O_2 fuel cells) have gained much attention due to their obvious advantages of high efficiency, low operating temperature, convenient operation, and no pollution [1–4]. On the other hand, for energy storage systems, metal–air batteries (such as lithium–air batteries and zinc–air batteries) are becoming attractive owing to their extremely high energy densities (their heoretical capacity is about three times that of the current commercial lithium-ion batteries) [5–10]. Nonetheless, the development of both the fuel cells and metal–air batteries are hurdled by their sluggish reaction in the cathodic oxygen reduction process. Therefore, developing high-performance cathode catalysts and enhancing their oxygen reduction reaction (ORR) ability are the major assignments for their promising industrial application [11,12].

Among many developed state-of-the-art ORR catalysts, Pt-based catalysts have showed excellent electrocatalytic activity [13,14]. However, due to their high price, instability and CO poisoning constitution, they are far from meeting the requirements of large-scale application [15–21]. At present, developing non-noble metal catalysts, such as transition metals (TMs) and their corresponding oxides, sulfides, carbides and nitride, etc., with high ORR activity to replace Pt-based catalysts is considered as a feasible solution [22–27]. Among them, TM single atomic catalysts (M_{SAC}) loaded on the nitrogen doped carbon (N-C) carriers derived from metal-organic frameworks (MOFs) exhibit amazing ORR activity and stability [28,29]. In M_{SAC}-N-C materials, strong metal-nitrogen coordination bonds prevent the dissolution, conglomeration, and exfoliation of TM atoms, making the TM dispersed atomically in M_{SAC}-N-C catalysts [30,31]. Therefore, the M_{SAC}-N-C catalysts possess many advantages including: (1) the type, size and proportion of the doped non-metallic elements can be well controlled by adjusting the preparation procedures of the MOF precursors; (2) the uniform porous structure of MOFs enables the carbon carriers to have a high specific surface area, which provides more loading sites for single atoms; (3) the high surface energy of single active atoms provides fast charge transfer, obtaining high catalytic activities.

Among the developed MOF precursors, zeolite imidazolate framework zinc salt (ZIF-8) has unique advantages. The aromatic methylimidazole ligand in ZIF-8 is rich in nitrogen (N/C molar ratio: 1/2), which can provide high density and uniform distribution of active sites in N-doped porous carbon materials. In addition, ZIF-8 has a caged pore structure, where the Zn-ions can be evaporated at high temperature above 900 °C. In that case, high density M-N_x monatomic active sites in the M_{SAC}-N-C catalysts can be obtained by one-step thermal activation process [32]. Moreover, in the M_{SAC}-N-C catalysts, the electron rearrangement in d-band of a single TM atom promotes adsorption and desorption of O_2, achieving high catalytic efficiency [33]. Therefore, using the ZIF-8 as carbon carrier precursor, more active TM atoms can be dispersed on the N-C carries to achieve high catalytic performance [34–36]. However, in spite of their outstanding catalytic performance, some challenges still need to be taken seriously: (i) It is generally believed that the thermodynamically stable structure for single atomic catalysts is one metal atom surrounded by four N atoms (M-N_4) [26,37,38]. However, some researchers proposed that the stable M-N_4 structure did not represent the highest catalytic activity [39,40]. Therefore, understanding the influence mechanism of coordination environments of TM single atom active centers and modulating the M_{SAC}-N-C structure are the key to designing and preparing high performance M_{SAC}-N-C catalysts. (ii) Researchers have pursues high loading amounts of TM atoms on the M_{SAC}-N-C catalysts to achieving enhanced catalytic performance, but too many single atoms too easily become agglomerated and form clusters, nanoparticles, oxides, or carbides with poor activity at high temperature. Although great efforts have been done achieve atomic dispersion of TMs on N-C matrix, the TM clusters or even nanoparticles are still inevitable in practical operation. Some researchers have proposed that the TM clusters or nanoparticles are also beneficial to catalysis [41–43]. Therefore, optimizing the single atom loading amounts is the key for preparation of high performance M_{SAC}-N-C catalysts. (iii) Some technological obstacles for their practical applications in fuel cells and metal air cells remain to be explored. There are still fewer works to evaluate the application performances of the Pt-free M_{SAC}-N-C catalysts in the devices, compare with testing using rotation disk electrode (RDE) measurement systems. The advantages and challenges of the M_{SAC}-N-C derived from ZIF-8 in ORR are summarized in Figure 1.

Figure 1. Summary diagram of the advantages and challenges of M_{SAC}-N-C catalysts derived from ZIF-8 precursors.

Considering this popular ORR catalyst and its recent important progress, herein, we present an updated review on ZIF-8 precursor derived M_{SAC}-N-C catalysts, based on their most challenges, including the coordination environments of single atoms in the ZIF-8 derived N-C matrix, advanced techniques for increasing the single atoms loading amount in M_{SAC}-N-C catalysts, and the applications of M_{SAC}-N-C catalysts in devices. Some perspectives regarding to the future research directions of M_{SAC}-N-C catalysts are also provided.

2. ZIF-8 Precursor

2.1. Structure of ZIF-8 Precursor

The chemical formula of ZIF-8 precursor is Zn[MelM]$_2$ (MelM is 2-methylimidazole), which consists of 2-methylimidazole and zinc atoms. As shown in Figure 2, each zinc atom coordinates with four nitrogen atoms on the 2-methylimidazole ring to form a Zn-N_4 cluster. By connecting imidazole rings on 2-methylimidazole, the ZIF-8 becomes a cage-like coordination compound with regular hexahedron crystals, and possesses some excellent structural features in high specific surface area, adjustable pore size, and pore functionalization [44,45]. During pyrolysis process, the evaporation of Zn can form N-doped porous carbon. Moreover, the rich nitrogen in the ZIF-8 can work as catchers to anchor the TM atoms during pyrolysis process, avoiding the agglomeration and exfoliation of TM atoms effectively [46].

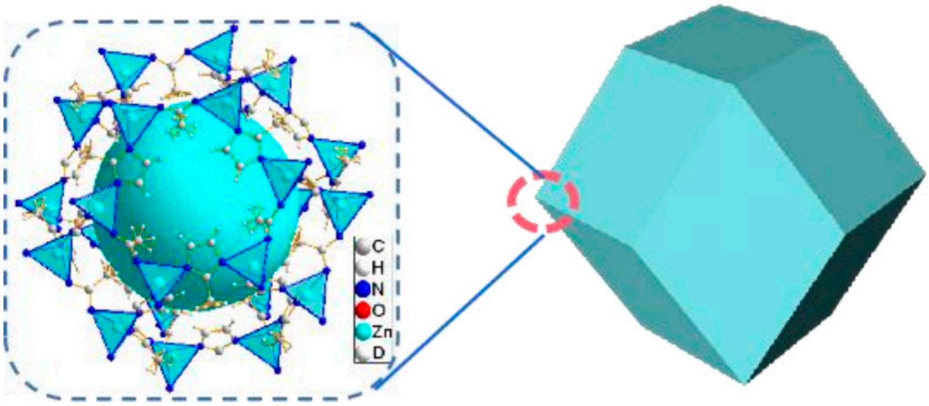

Figure 2. Schematic diagram of ZIF-8 structure.

2.2. Preparation of ZIF-8 Precursor

Good synthetic methods for ZIF-8 are of great significance to improve the quality of M_{SAC}-N-C catalysts and reduce their cost. Here, we aim to selectively introduce two common preparation methods of ZIF-8 precursor, i.e., solvothermal method and liquid phase diffusion method. These two representative preparation methods have the advantages of facile preparation and good quality of ZIF-8 production.

2.2.1. Solvothermal Method

The solvothermal preparation process is usually realized by dissolving the zinc nitrate and organic imidazole ligand into a mixed solvent of N, N-dimethylformamide (DMF) and N, N-dimethylacetamide (DEF), followed by heating the sealed solvothermal reaction vessel containing the above solution to more than 90 °C for more than 24 h. After solvothermal reaction, the obtained precipitation powder is ZIF-8. Hayashi et al. synthesized ZIF-8 precursor by dissolving zinc nitrate and 2-methylimidazole (with a molar ratio of 1:1) in DMF solvent and reacting at 140 °C for 24 h [47]. The synthesized ZIF-8 showed excellent thermal and chemical stability. The preparation procedure of the solvothermal method is relatively simple, but it usually takes a long reaction time. Additionally, the solvent molecules tend to block the pores of ZIF-8, making purification of ZIF-8 difficult.

2.2.2. Liquid Phase Diffusion Method

The liquid phase diffusion method is more widely used than the solvothermal method to prepare ZIF-8, because the liquid phase diffusion method can be carried out at room temperature [48]. The most common procedure of liquid phase diffusion method is dissolution of zinc nitrate and organic ligands in methanol solvent. Then, by stirring, the ZIF-8 precipitation can be obtained.

Li et al. successfully obtained a well-designed nanosized ZIF-8 precursor with a uniform crystal size of about 78.6 nm via combining ultrasonic dispersion treatment with a room temperature solution reaction [45]. Through high temperature pyrolysis, the hierarchical nanoporous N-doped carbon ZNC-1000 electrocatalyst was prepared, which possessed large surface areas and led to sufficient exposed electrochemical active sites, as well as moderate graphitization degree and suitable hierarchical pores distribution, resulting in the sufficient interaction between O_2 and the electrocatalyst surface.

Venna et al. reported the structural evolution of ZIF-8 in methanol solvent as a function of time at room temperature and identified the different stages of ZIF-8 formation (nucleation, crystallization, growth, and stationary periods) [49]. They hypothesized that the observed semicrystalline-to-crystalline transformation may take place via solution- and solid-mediated mechanisms, as suggested by the observed phase transformation evolution and Avrami's kinetics, respectively. ZIF-8 forms a complete crystalline phase before the formation of long-range ordered crystals, which demonstrated that the substances involved in the synthesis of ZIF-8 in methanol solution may form an intermediate structure and then develop a growth structure through the solution-transport or solid-state (Avrami kinetic support) transformation mechanism.

Bustamante et al. investigated the effect of the solvent on the synthesis process and on the nanocrystal characteristics of the ZIF-8 [50]. A synthesis protocol at room temperature employing a series of aliphatic alcohols, water, dimethylformamide and acetone was employed. The results showed that the solvent modifies the evolution of the reaction, altering the crystallization rates and nanocrystal sizes. The materials obtained in methanol and N-octanol showed the highest crystallinity and crystallite size, which was suitable solvent to modify the synthesis process and the nanocrystal characteristics of ZIF-8. When synthesized in alcohol and acetone, these nanocrystals formed globular aggregates with large sizes. In contrast, under the same synthesis conditions, when using water or dimethylformamide, the ZIF-8 phase was not developed. In alcohols other than methanol, the crystals developed pill-shaped morphologies with poorly defined facets.

3. The Coordination Environments of TM Single Atoms in M_{SAC}-N-C

The carbon derived from ZIF-8 precursor contains a large amount of pyridine nitrogen and micropores. The pyridine nitrogen can effectively anchor the TM atoms to form catalytic active sites by TM-N coordination; while the porous structure can facilitate the mass transfer and adsorption ability of O_2, thus improving the current density and the catalytic activity of M_{SAC}-N-C catalysts [51]. Therefore, the M_{SAC}-N-C catalysts usually have better catalytic activity than the traditional bulk- or nano-catalysts [52]. It is generally believed that the four-electron ORR reaction in an alkaline environment usually undergoes the following five steps [53]:

i. $O_2(g) + * \rightarrow O_2^*$
ii. $O_2^* + H_2O(l) + e^- \rightarrow OOH^* + OH^-$
iii. $OOH^* + e^- \rightarrow O^* + OH^-$
iv. $O^* + H_2O(l) + e^- \rightarrow OH^* + OH^-$
v. $OH^* + e^- \rightarrow OH^- + *$

(* denotes adsorption position).

Various coordination environments of TM atoms in the M_{SAC}-N-C catalysts lead to different degrees of four-electron ORR reaction. Researchers usually analyze the coordination environment of TM atoms in M_{SAC}-N-C by combination with the characterizations of X-ray Photoelectron Spectroscopy (XPS), X-ray Absorption Spectroscopy (XAS), and Mössbauer

Spectrum, and calculate the ORR reaction activation energy by Density Functional Theory (DFT) to further determine and optimize the coordination of TM atoms in the M_{SAC}-N-C. They found that tuning the coordination environments of TM atoms could effectively enhance the catalytic activity of the M_{SAC}-N-C.

3.1. Effect of M_{SAC}-N_4 Spin States

In the M_{SAC}-N_4-C structure, there are two kinds of coordination structures according to different spin state of the active center atoms. Xiao et al. proposed that the Fe in the Fe-N-C catalyst derived from Fe-ZIF-8 precursor exhibited two coordination environments with nitrogen, one is D1 coordination structure with low-spin Fe^{2+}-N_4, another is D2 coordination structure with medium-spin Fe^{2+}-N_4 or high-spin O_x-Fe^{3+}-N_4 [54]. The in situ X-ray absorption near edge structure (XANES) results illustrated that the D2 coordination structure underwent an Fe^{3+}/Fe^{2+} transition during ORR process, and the active site nonplanar HO-*Fe($^{2+}$)-N_4 formed spontaneously and exhibited an ultrahigh turnover frequency of 1.71 e s^{-1} $sites^{-1}$, thus achieving higher ORR performance. Xu et al. prepared the Fe-N-C catalyst from Fe-doped ZIF-8 precursor using a microwave-assistant method (M_{15}-FeNC-NH_3) [55]. They also proved that there are two kinds of Fe-N_4 active sites in the M_{15}-FeNC-NH_3 by Mössbauer spectrum (Figure 3a). By calculating the free energy evolution of ORR, they found that the activation energies of two kinds of Fe-N_4 coordination (D1 and D2 shown in Figure 3a) for ORR are different. As shown in Figure 3b, the rate-limiting step energy barrier for D1 (0.29 eV) is much lower than that of D2 (0.43 eV), indicating that the Fe-N_4 coordinated as D1 type is more beneficial for ORR.

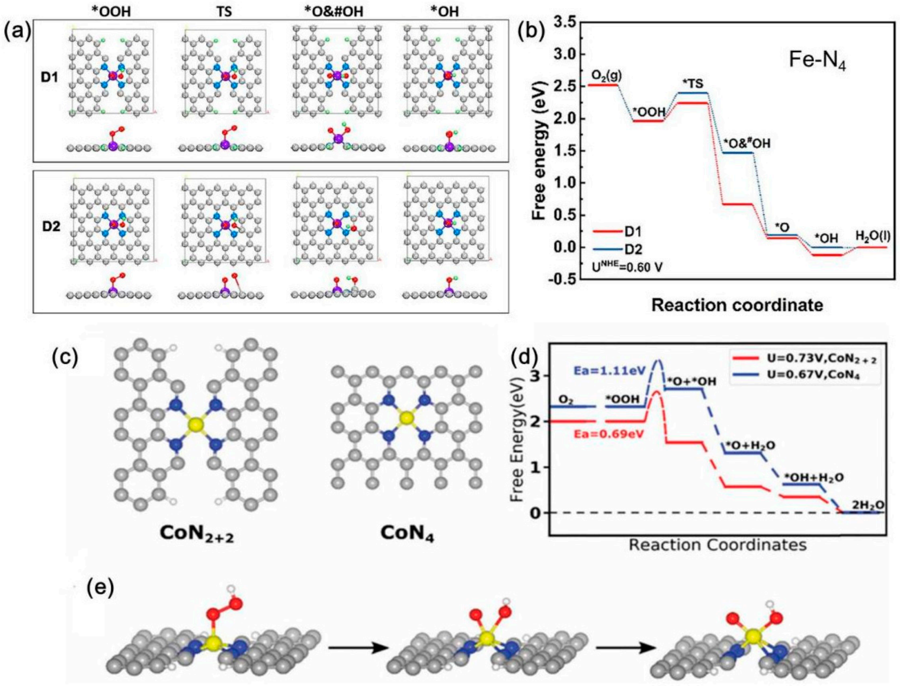

Figure 3. DFT calculations. (**a**) Structures of optimized configurations of adsorbed species on Fe-N_4 with D1 and D2 sites, H: green, C: grey, O: red, N: blue, Fe: purple; (**b**) free energy diagrams for the ORR on the Fe-N_4 D1 and D2 sites, Reproduced with permission from Ref. [55], Elsevier: 2021; (**c**) atomic structures of Co-N_{2+2} and Co-N_4 active centers of Co-N-C catalyst; (**d**) the free energy evolution diagram of $4e^-$ ORR pathway was calculated at the limiting electrode potential U = 0.73 V and the limiting electrode potential U = 0.67 V. (**e**) atomic structure of the initial (left), transition (middle) and final (right) states of the dissociation reaction at the Co-N_{2+2} (where the gray, blue, yellow, red and white spheres represent C, N, Co, O and H atoms, respectively), Reproduced with permission from Ref. [56], Royal Society of Chemistry: 2019.

Similar to Fe-N-C, the Co-N-C catalyst derived from Co-ZIF-8 precursor also has two kinds of Co-N coordination structures. He et al. prepared the surfactants modified Co-N-C catalysts, and found that both Co-N_4 and Co-N_{2+2} coordination structures existed in the Co-N-C [56]. The DFT results (Figure 3c–e) showed that both Co-N_4 and Co-N_{2+2} could trigger the ORR reaction by binding O_2. However, during the rate limiting *OOH dissociation step, the reaction at the Co-N_{2+2} site has much lower activation energy (0.69 eV) than that at the Co-N_4 site (1.11 eV). Therefore, the Co-N_{2+2} could achieve the ORR with $4e^-$ electron transfer, but the Co-N_4 could not be due to the high activation energy. This research also demonstrates that the Co-N-C catalyst derived from ZIF-8 possesses more Co-N_{2+2} active sites, which can improve the selectivity and activity of ORR with $4e^-$ transfer in both alkaline and acidic electrolytes. The authors further optimized the conditions for the formation of active Co-N_{2+2} sites, and found that the critical transition occurs at 700 °C and becomes optimal at 900 °C [57].

3.2. Unsaturated M_{SAC}-N_x Coordination

Recently, many studies have confirmed that the unsaturated M_{SAC}-N_x ($x < 4$) coordination environment in the M_{SAC}-N-C can lower the O_2 adsorption energy barrier, which will facilitate the ORR catalytic activity. Fan et al. investigated the effect of coordination of Pt-N on the ORR performance for Pt-N_x-C ($1 \leq x \leq 4$) catalyst [39]. By controlling the carbonization temperature of the Pt-ZIF-8 precursor, they obtained Pt-N_x-C with various N coordination number. The experiment and DFT calculation results showed that the catalytic order for the Pt-N_x-C is Pt-N_1-C > Pt-N_2-C > Pt-N_3-C > Pt-N_4-C. This catalytic activity order mainly depends on the ability of absorption between Pt and *OOH.

Moreover, owing to low overpotentials of Cu-N catalytic centers, Cu-N-C catalysts have also attracted much attention for ORR [26,40]. Ma et al. innovatively proposed that decreasing the N coordination number of Cu active center (Cu-N_3) could enhance the ORR catalytic activity [40]. They developed an ionic exchange strategy to fabricate the unsaturated Cu-N_3 centers. The DFT calculation result revealed that the O_2 adsorption energy barrier for CuN_3 (0.17 eV) was much lower than that of CuN_4 (0.87 eV), demonstrating the high ORR activity for the unsaturated Cu-N_3 centers.

3.3. Regulation of Electronic Density

In addition to reducing the M-N binding number, the researchers also found that the ORR catalytic activity of M_{SAC}-N-C can be further improved by regulating the electronic density of the central metal atoms. Controlling the N-C structure to modify the M_{SAC}-N-C is one of the good examples. Ha et al. proved that the pyridinic N is beneficial to catalytic performance of the Co-N-C catalyst, and the Co-pyridinic N-C structure can be obtained by introducing lysozyme during the synthesis process [58]. The optimized Co-pyridinic N-C exhibited an enhanced ORR catalysis activity with positive $E_{1/2}$ of 0.87 V and 0.83 V in alkaline and acidic media, respectively, surpassing regular Co-N-C catalysts. Im et al. tuned the Co-ZIF-8 precursor by encapsulating melamine [59]. They found that the melamine modification could enhanced oxophilicity of the Co-N4 active site toward the axial coordination environment, achieving higher catalytic activity and stability compared to the other transition metals. Chen et al. demonstrated the electronic density of Co active sites in the Co-N-C derived by Co-ZIF-8 can be tailored through regulating atomic coordination environments [60]. A sulfur and phosphorus co-modified Co-N-C (Co_1-N_3PS/HC) catalyst was designed and synthesized. The synergistic coordination of N, P, and S to atomically dispersed Co active centers played a crucial role of optimized electronic density of Co-N-C catalyst and remarkable enhanced its ORR performance.

In addition to Co-N-C system, Pt-N-C catalyst can also be modified by adjusting its electronic structure. Song et al. prepared Pt-N-C catalyst using atomic layer deposition of Pt atoms on the ZIF-8 derived N-C framework [61]. They found that the electronic structure of Pt-N-C could be adjusted by adsorption of hydroxyl and oxygen, which greatly lowered free energy change for the rate-limiting step and enhanced the ORR activity.

4. Strategies to Increase the Active TMs Loading

Pursuing more active TM single atoms loading amount is the trend to improve the catalytic performance of M_{SAC}-N-C catalyst. However, owing to the high energy, the single atoms are easy to agglomerate during high-temperature pyrolysis process to form fewer active species, such as metal clusters, nanoparticles, oxides, or carbides. Recently, on the one hand, researchers developed advanced synthesis technologies for constructing M_{SAC}-N-C with more active single atom loading; On the other hand, the beneficial effects of metal clusters and nanoparticles on the ORR catalysis for M_{SAC}-N-C catalysts are constantly being explored.

4.1. Advanced Techniques for Preparing M_{SAC}-N-C with High M_{SAC} Loading

4.1.1. Bimetal Node Doping Strategy

Zinc-based bimetallic ZIF-8 has been most widely used in bimetal node doping strategy [32,62]. During the preparation process, TM ions with catalytic activity (such as Co^{2+}, Ni^{2+}, Fe^{2+}, etc.) are added into the solution together with Zn^{2+}. In that case, Zn^{2+} and TM ions can coordinate with 2-methylimidazole and evenly distribute in the ZIF-8 matrix by the anchoring effect of nitrogen to form bimetallic dispersion. In the following heat treatment process, the zinc atoms are vaporized due to their low boiling point (~906 °C), leaving a lot of vacancies on the M_{SAC}-N-C. Such vacancies further separate the TM atoms, thus avoiding the agglomeration of TM single atoms on the M_{SAC}-N-C.

Wang et al. achieved stable cobalt (Co) single atoms dispersed Co-N-C by this bimetal node doping strategy [63]. As shown in Figure 4a, the authors firstly designed a (Zn, Co)-ZIF-8 with uniform distribution of zinc and Co atoms on ZIF-8 matrix, and then removed the Zn atoms by heating the compound up to 1000 °C. The obtained Co-N-C retained the dodecahedron morphology of its ZIF-8 precursor (Figure 4b,c) with a loading amount of Co more than 4 wt%. By detection of EDX, they found that the Co atoms distributed homogeneously throughout the structure of Co-N-C catalyst (Figure 4d). The HAADF-STEM and SAED techniques further observed directly that there were no cobalt crystals in the Co-N-C (Figure 4e–g), indicating that the Co atoms remained atomic dispersion after pyrolysis.

4.1.2. Space Constraint Strategy

In this method, the micropores on the surface of ZIF-8 are used to seize the TM atoms and prevent them migration and agglomeration. The key to this method is to select an appropriate TM precursor with the molecular size smaller than the micropores of ZIF-8, but larger than half of the diameter of micropores. This ensures that only one TM precursor is embedded in each micropore of ZIF-8 [54]. Chen et al. prepared Fe-ISAS/C-N catalysts with a Fe loading amount up to 2.16 wt% through this space constraint strategy [53]. The experimental schematic details are shown in Figure 5a. They used iron acetate [$Fe(acac)_3$] as the TM precursor, which can be captured in a ZIF-8 pore (pore diameter (dp) of ZIF-8 is 3.4Å) by the size effect. After pyrolysis, the Fe-ISAS/C-N catalyst was obtained. The XANES and EXAFS results confirmed that separated Fe atoms were anchored in C-N matrix by $Fe-N_4$ coordination (Figure 5b–f). The authors also calculated the free energy of the four-electron ORR reaction by DFT. The calculation results showed that the reactivity of ORR was mainly restricted by the step of *OH accepted electrons to form OH^-. Due to easier transfer of electrons from Fe single atom to the adsorbed *OH, the Fe-ISAS/C-N exhibited much lower over-potential of 0.65 V than that of the Fe cluster catalyst (1.76 V).

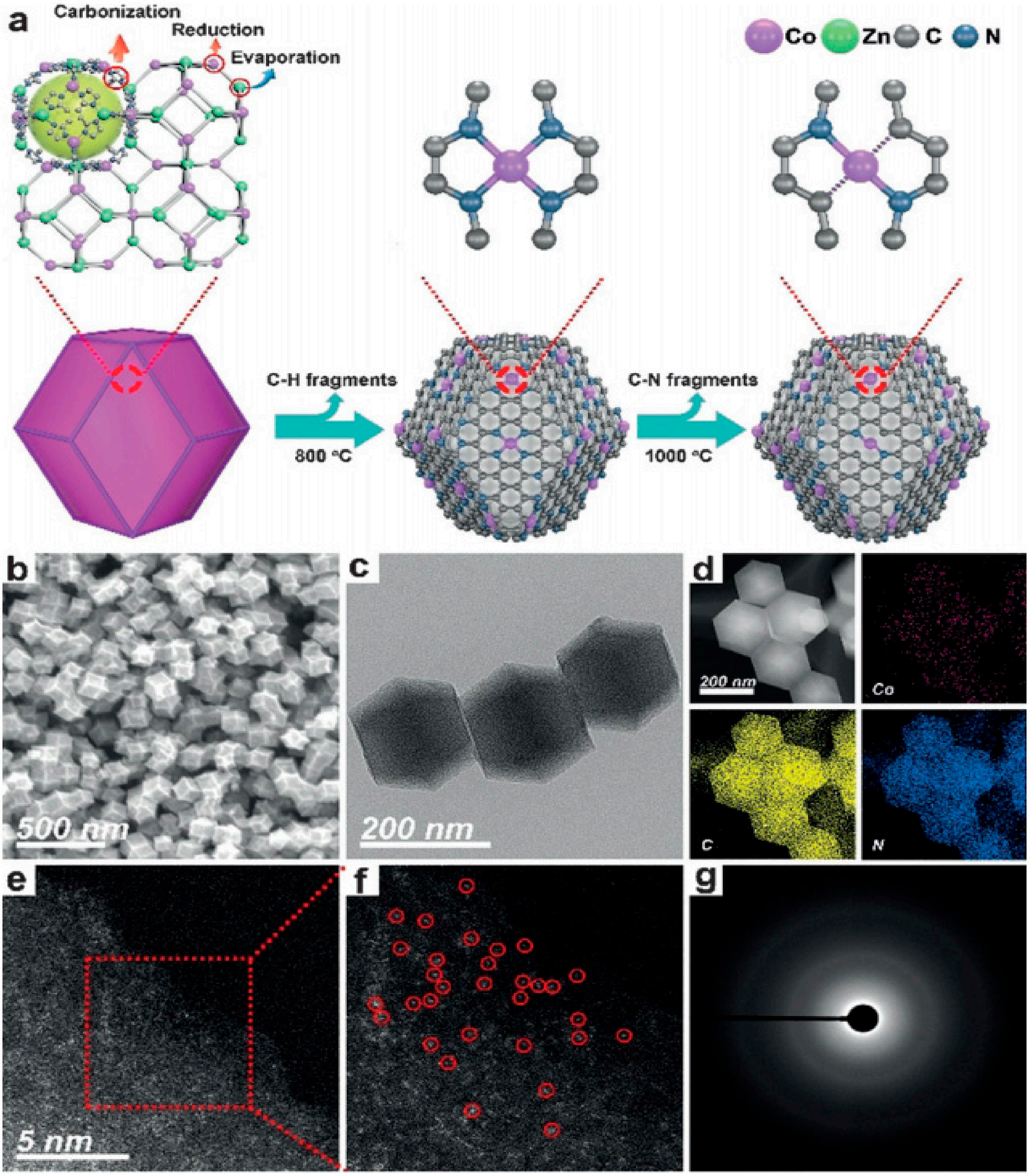

Figure 4. Bimetal Node Doping Strategy. (**a**) The schematic preparation process of Co-N-C by the bimetal node doping strategy; (**b**) scanning electron microscopy (SEM), (**c**) transmission electron microscopy (TEM), (**d**) energy dispersive X-ray spectroscopy (EDX), (**e**,**f**) high-angle dark field scanning transmission (HAADF-STEM) and (**g**) selected area electron diffraction (SAED) images of Co-N-C sample. Reproduced with permission from Ref. [63], John Wiley & Sons Ltd.: 2018.

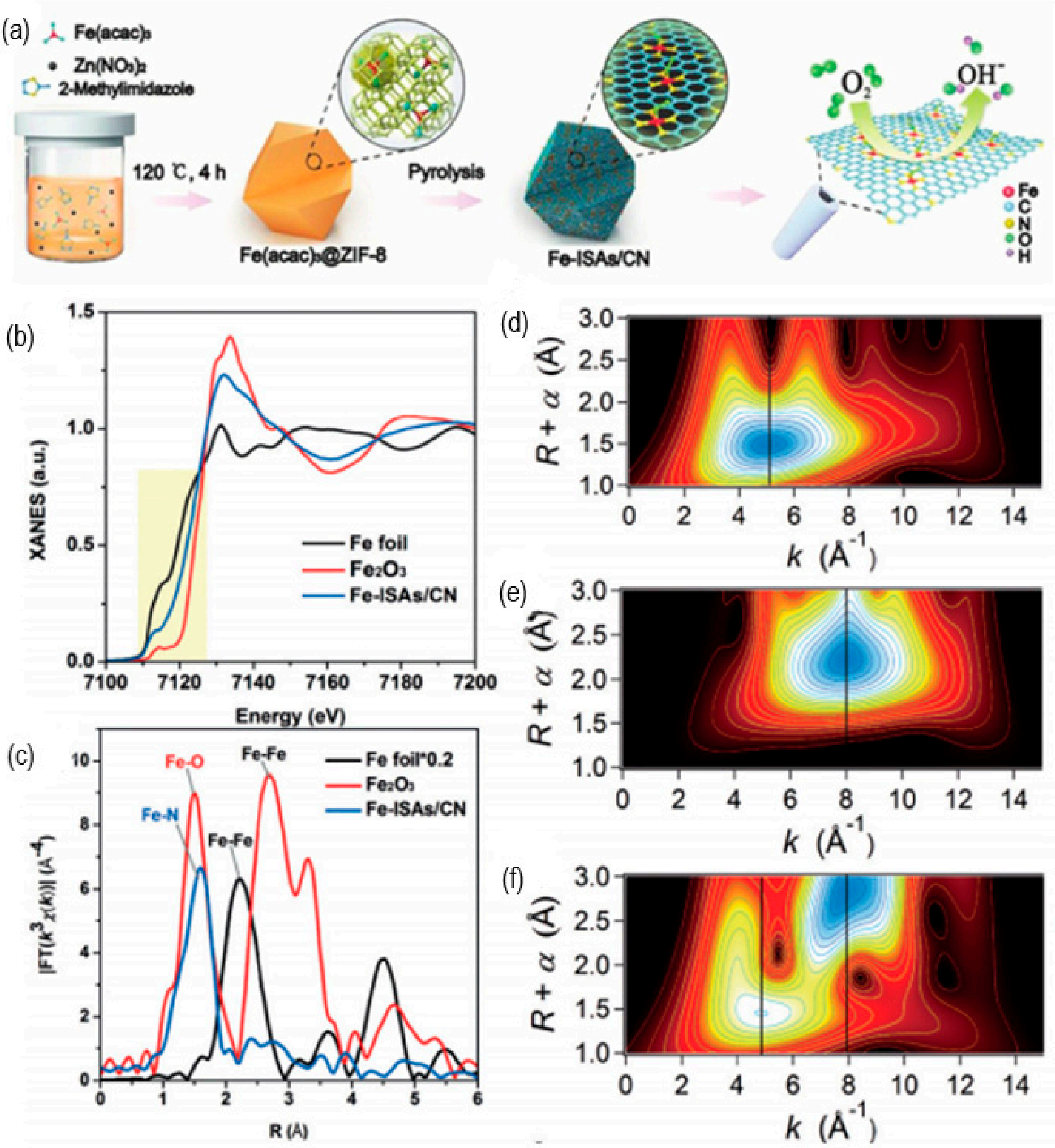

Figure 5. Space Constraint Strategy. (**a**) Schematic diagram of Fe-ISAS/C-N preparation by space constraint strategy; (**b**) X-ray absorption near edge structure (XANES) spectra (yellow region highlights near side energy absorption); (**c**) corresponding X-ray absorption fine structure (EXAFS) curves of Fe-ISAS/C-N; and Fe K-edge Fourier transform (FT) and Wavelet transform (WT) for (**d**) Fe-ISAS/C-N, (**e**) Fe foils, and (**f**) Fe_2O_3 samples. Reproduced with permission from Ref. [53], John Wiley & Sons Ltd.: 2017.

4.1.3. Surfactant Coating Strategy

Although great advances have been made in synthesis of M_{SAC}-N-C catalysts, further enhancement of the density of active single atoms is still a challenge [64]. Increasing the content of TM during the preparation process directly will lead to the serious agglomeration of TM. Recently, He et al. reported a new method to increase the density of Co single atoms by introducing surfactants [56]. They found that the surfactants can not only contribute to single atomic dispersion, but also prevent the collapse of ZIF-8 porous structure during the pyrolysis process. Among many comparative surfactants, the poloxham (F127) showed the best modification effect. The modified Co-N-C@F127 exhibited an excellent ORR activity even in acidic electrolyte, which should be attributed to the increased single Co density (from 0.9 at.% for the surfactant-free Co-N-C to 1.0 at.% for the Co-N-C@F127).

4.1.4. Other Strategies for Synthesis of M_{SAC}-N-C

Except the common strategies mentioned above, although some other strategies for preparing single atomic catalysts may be obviously limited by the reaction of substances and condition, these innovative findings provided new pathways for the integrated engineering of geometric or electronic structures of single-atom materials to improve their catalytic performance.

Jiang et al. prepared atomically dispersed Fe−N_4 sites anchored on three-dimensional (3D) hierarchically porous carbon by precisely atomic-level control, which possessed well defined single-atom sites (SAs), adjustable mass loadings and enhanced active-site accessibility [65]. With 0.20 wt.% of nonprecious metal, the Fe SAs-N/C-20 catalyst exhibited superior ORR performance with a half-wave potential ($E_{1/2}$) of 0.915 V (vs RHE) in 0.1 M KOH. Density functional theory (DFT) results illustrated that hierarchical carbon pores successfully optimize the electronic structure of Fe−N_4 by changing the local coordination of pyridine-like N, which enables the selective C−N bond cleavage (SBC) adjacent to Fe centers to form edge-hosted Fe−N_4 moieties, and therefore lowers the overall ORR barriers to acquire excellent activity and long-term durability.

Qu et al. conducted a gas-migration/NH_3-mediated strategy that transformed bulk transition metals into M_{SAC}-N-C was developed and validated, where ammonia molecules served as a medium to haul out copper atoms and anchor them to the volatilized zinc nodes of the ZIF-8 at high temperature [66]. The resultant Cu-SAs/N-C catalyst could endow superior ORR performance and exceptional electrochemical and thermal stability, and the generality of this approach and critical role of the ammonia molecules were also confirmed to provide valuable guidance for the direct preparation of M_{SAC}-N-C from non-precious bulk metals.

Shang et al. developed a mSiO_2-protected calcination strategy for the synthesis of hierarchically porous Co,N-CNF electrocatalysts from Co,N-ZIF precursors [67]. This protection strategy yielded high specific surface area Co,N-CNF products with graphitic carbon character, and further allowed good control over the specific surface area and availability of catalytic active sites through variation of the pyrolysis temperature. The Co,N-CNF products possessed outstanding ORR catalytic activity, superior to Pt/C at the same loading in alkaline media and comparable to Pt/C in acidic media. Considering its low-cost, very positive ORR onset and half-wave potential, excellent durability, and absolute immunity to methanol crossover, Co,N-CNF is a very promising candidate to replace Pt/C in the practical fuel cell applications.

Zhou et al. developed a negative pressure pyrolysis strategy that allowed to controllably prepare series of single metal sites supported on three-dimensional graphene frameworks with high accessibility and stability, which greatly increased the utilization and catalytic efficiency of the supported metal atoms [68]. The findings not only opened up a new way of preparing highly accessible single site catalysts, but also provided an understanding of defect engineering of single metal sites to enhance their catalytic performance.

Liu et al. presented a direct ZIF-8 thermal melting strategy to synthesize 2D structured single iron atoms anchored on porous graphene nanosheets [69]. The s-Fe/ZIF-8 was tightly embedded in GO. During the high-temperature treatment, it suffered from thermal melting on the graphene sheets and then pyrolysis, resulting in porous ultrathin carbon layer on graphene sheets. More importantly, abundant Fe-N_x active sites were anchored in the ultrathin carbon layer, making the single atom Fe active sites on the surface and realizing their fullest utilization. As a result, the as-prepared Fe-N/GNs exhibited efficient and stable ORR performances in both alkaline and acidic mediums.

4.2. Beneficial Effects of Metal Clusters and Nanoparticles on M_{SAC}-N-C Activity

It is generally believed that single atomic catalysts possess much higher catalysis efficiency than that of the metal clusters and nanoparticles [70]. However, during the practice fabrication process of the M_{SAC}-N-C catalysts, it is difficult to avoid the formation of metal clusters or nanoparticles due to the high activity of single TM atoms. Fortunately, increasing numbers of researchers have proved that the synergistic effect of metal nanoclusters or nanoparticles and single atom can promote the ORR catalytic activity of M_{SAC}-N-C catalysts [43,71,72].

4.2.1. Synergistic Effect of Metal Clusters and Single Atoms

Although the catalytic performance of metal clusters themselves has been proved to not be as robust as the single atomic catalysts, their existence in the M_{SAC}-N-C system is beneficial to improve the activity of single atoms. Ao et al. designed a Fe-N-C catalyst with both Fe single atoms and Fe nanoclusters embedded in the N-C matrix (Fe_{AC}@Fe_{SA}-N-C) [71]. They found that the Fe_{AC}@Fe_{SA}-N-C catalyst had better ORR activity (with half-wave potential of 0.912 V vs. RHE) than that of Fe_{SA}-N-C (with half-wave potential of 0.844 V vs. RHE). The DFT calculation proved that extra Fe atom/cluster (Fe_1 and Fe_{13}) could enhance the activity of Fe-N_4 active sites. Wang et al. also found the synergistic phenomenon of Fe single atoms and Fe nanoclusters for ORR catalysis, and proposed the modification mechanism that Fe clusters can break the symmetric electronic structure of Fe-N_4 [73]. Moreover, the 3d orbitals of Fe single atomic centers could be optimized by introducing Fe clusters and other atoms (such as sulfur), leading to acceleration of the rate limiting step of ORR by breaking the O-O bond in OOH* (Figure 6a,b). Wang et al. achieved a Mo-based Mo-N-C_2 catalyst by using a cage-controlled pyrolysis route [74]. In the Mo-N-C_2 catalyst, the Mo has the size ranging from isolated single Mo atom to subnanometer clusters (less than 1 nm). They also investigated the ORR electrocatalytic behavior of Mo with the size from Å to nanometer scale by carefully control of dispersion of precursors. The EXAFS analysis combined with theoretical calculation demonstrated that the local coordination environment of Mo in Mo-N-C_2 catalyst could promote both the ORR and OER performances.

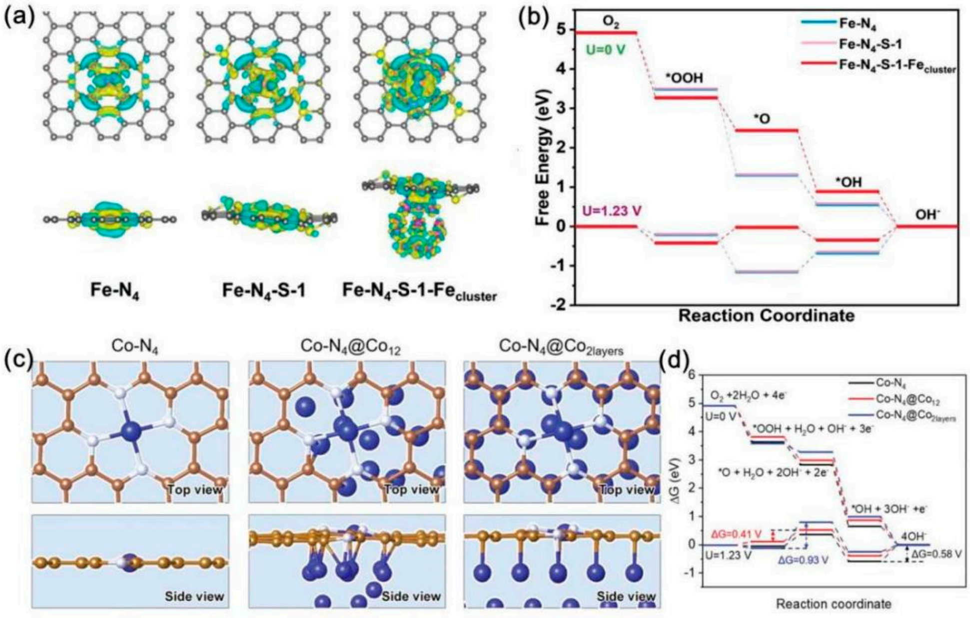

Figure 6. DFT calculations of (**a**) charge densities (yellow: electron accumulation, cyan: electron depletion) (**b**) free energis at U = 0 V, and 1.23 V for Fe-N_4, Fe-N_4-S-1, and F-N_4-S-1-$Fe_{cluster}$. Reproduced from Ref. [73], John Wiley & Sons Ltd.: 2022 (**c**) Top views and side views of the optimized atomic structures of Co-N_4, Co-N_4@Co_{12}, and Co-N_4@$Co_{2layers}$; (**d**) ORR free energy for Co-N_4 (black line), Co-N_4@Co_{12} (red line), and Co-N_4@$Co_{2layers}$ (blue line) at U = 0 V, and 1.23 V along 4-electrons pathway. Reproduced from Ref. [75], John Wiley & Sons Ltd.: 2021.

4.2.2. Synergistic Effect of Nanoparticles and Single Atoms

The phenomenon of strong interaction with single atomic sites and promoting their catalytic activity is also exhibited for the nanoparticles. Wang et al. prepared Co single atoms in the form of Co-N_4 and Co nanoparticles co-anchored on N-C framework (Co-SAs/SNPs@NC) [75]. Their DFT calculation results reveal that Co nanoparticles can increase the valence state of the Co single atoms in Co-SAs/SNPs@NC and moderate the adsorption free energy of ORR intermediates (Figure 6c,d).

Additionally, by heating the Fe-ZIF-8 precursor in NH_3 atmosphere, Liu et al. got Fe_2N nanoparticles decorated Fe-N-C catalyst (Fe-N-C/HPC-NH_3) [43]. They analyzed the adsorption free energies of FeN_4-Fe_2N, FeN_4 and Fe_2N species, the results showed that FeN_4-Fe_2N could weaken the adsorption of ORR intermediates and reduce the energy barrier of the rate-limiting step, hence improving the ORR activity.

5. ORR Performances of M_{SAC}-N-C Catalysts Applied in Devices

The M_{SAC}-N-C catalysts derived from M-ZIF-8 precursors usually exhibit better catalytic activity than that of the traditional bulk- or nano-catalysts, due to there are a large amount of pyridine nitrogen and micropores in the structure of M_{SAC}-N-C catalysts. The pyridine nitrogen is beneficial for anchoring the TM atoms on the N-C matrix by TM-N coordination, while the porous structure can facilitate the mass transfer and adsorption ability of O_2, thus improving the current density of M_{SAC}-N-C catalysts [51,52]. So far, many kinds of M_{SAC}-N-C catalysts derived from M-ZIF-8 precursors have been reported to boost the ORR kinetics. Some typical M_{SAC}-N-C catalysts with single and double TM atoms are summarized in Figure 7. However, the M_{SAC}-N-C catalysts used in devices, such as fuel cells or metal air batteries, are not much enough. This section focusses on the ORR performances of M_{SAC}-N-C catalysts applied as the air cathode for fuel cells and zinc-air batteries.

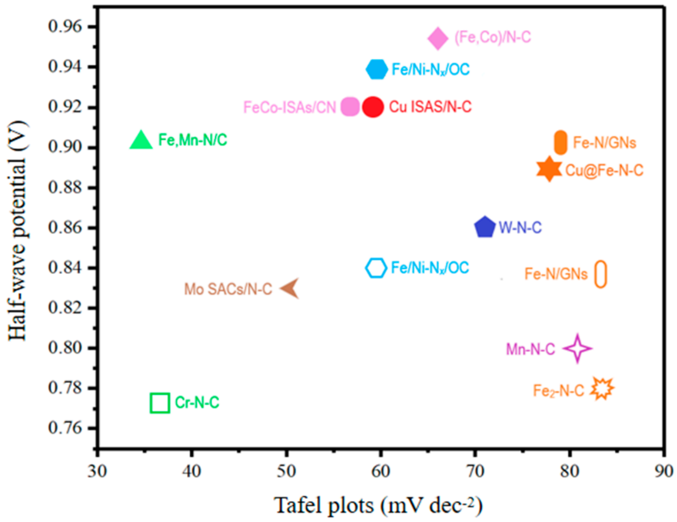

Figure 7. The comparison of ORR performances of M_{SAC}-N-C catalysts derived from ZIF-8 (solid points express the performance in alkaline electrolyte, hollow points express the performance in acidic electrolyte). (Fe-N/GNs [69], Mn-N-C [76], Cr-N-C [77], W-N-C [78], Mo SACs/N-C [74], Cu ISAS/N-C [79], Fe_2-N-C [42], Cu@Fe-N-C [80], (Fe,Co)/N-C [81], FeCo-ISAs/CN [82], Fe/Ni-N_x/OC [83], Fe,Mn-N/C [84]).

5.1. *M_{SAC}-N-C Catalysts Applied for Fuel Cells*

Among many M_{SAC}-N-C candidates, the Fe-N-C catalysts with Fe as the active catalysis center have been most studied as the air cathode for fuel cells due to their durability and high ORR activity [85,86]. For example, Xu et al. prepared the Fe-N-C catalyst from ferrocene-ZIF-8 precursor and applied it in a H_2-O_2 fuel cell as cathode ORR catalyst, with Pt/C as anode catalyst [87]. The maximum power density of 601 mW cm^{-2} and a current density of 380 mA cm^{-2} at 0.7 V were obtained. Qiao et al. modified the Fe-N-C catalysts by carbonizing the Fe-doped ZIF-8 single crystals, and finally obtained an FeN_4-doped hierarchical ordered porous carbon (FeN_4/HOPC) skeleton [88]. In proton-exchange membrane H_2-O_2 fuel cell, the optimal catalyst FeN_4/HOPC-c-1000 reached 420 mW cm^{-2} at a cell voltage of 0.57 V, and a current density of 690 mA cm^{-2} at 0.6 V. Deng et al. prepared a hollow nanopolyhedron catalyst (C-FeHZ8@g-C_3N_4) using the iron acetyl acetone and g-C_3N_4 doped ZIF-8 as raw materials [89]. This C-FeHZ8@g-C_3N_4 catalyst showed superior ORR activity in both acidic ($E_{1/2}$ = 0.78 V) and alkaline ($E_{1/2}$ = 0.845 V) electrolyte solutions. When working as the cathode catalyst in the H_2-O_2 fuel cell, the maximum power density of the fuel cell could reach to 628 mW cm^{-2} [89].

Despite the Fe-N-C catalysts possess encouraging ORR activity for fuel cells, the Fenton reaction of Fe-based catalysts are still hard to avoid [76,90]. The Fenton reactions involves generation of H_2O_2 via the two-electron ORR and generation of radical oxygen species [91]. Both of them could attack the FeN_4 active sites, thereby accelerating performance degradation [57]. Therefore, other TMs, such as Co, Ni and Mn have also been studied to work as catalyzing active center atoms in M_{SAC}-N-C. He et al. prepared Co-N-C catalyst from Co-ZIF-8 precursor, and tested in a H_2-air fuel cell [57]. The Co-N-C cathode catalyst displayed a peak power density of 390 mW cm^{-2}. After 15 000 cycles accelerated stress test, the voltage drop at a current density of 0.8 mA cm^{-2} was only 10 mV, indicating good durability. Chen et al. synthesized a series of Co-N-C catalysts with different CoN_4 densities [36]. The power density showed a slow linear increase in the low concentration region and an accelerated increase in the high concentration region of CoN_4 active sites, demonstrating the crucial role of the high active site density to the high power density of Co-N-C. When 1.6%CoNC@ArNH_3 was measured under H_2/air PEMFC condition, it displayed considerable peak power densities of 826 mW cm^{-2}, and also exhibited good stability at the constant voltage of 0.5 V. Li et al. prepared Mn-N-C catalyst with the atomically dispersed Mn-N_4 moieties embedded in the carbon surface-exposed basal planes, which exhibited an $E_{1/2}$ of 0.80 V vs. RHE, along with good stability in acidic media [76]. Then, the catalyst was further studied as a cathode in membrane electrode assemblies (MEAs) for H_2-O_2 fuel cells, which was capable of generating current densities of 0.35 and 2.0 A cm^{-2} at 0.6 and 0.2V, respectively, at a reasonable 1.0 bar partial pressure. The corresponding power density was up to 0.46 W cm^{-2}, demonstrating an alternative concept to develop robust and highly active PGM-free catalysts as replacements for Fe catalysts.

In order to directly compare the performances of various M_{SAC}-N-C catalysts for fuel cell, some typical M_{SAC}-N-C catalysts performances are summarized in Table 1.

Table 1. The performance of fuel cells with recently reported M_{SAC}-N-C catalysts derived from ZIF-8.

Samples	Types of Fuel Cells	Catalyst Loading Density [mg cm^{-2}]	Peak Power Density (mW cm^{-2})	Durability (h)	Ref.
Fe-N-C	H_2-O_2 fuel cell	0.5	601	12	[87]
FeN_4/HOPC	H_2-O_2 fuel cell	-	420	100	[88]
C-FeHZ8@g-C_3N_4	H_2/O_2 PEMFC	4	628	8	[89]
Co-N-C@C_{F127}	H_2-O_2 fuel cell	4.0	870	100	[56]
Co-N-C	H_2/air cell	4.0	390	27	[57]
CoNC-ArNH_3	H_2/O_2 PEMFC	3	826	20	[36]
20Mn-N-C	H_2/O_2 fuel cell	4.0	460	-	[76]
Z8@DA-FIP-950-C	H_2/O_2 PEMFC	3	454	25	[85]
(Fe,Co)/N-C	H_2/O_2 fuel cell	~0.77	505	100	[81]
Fe/Ni-N_x/OC	H_2/O_2 PEMFC	1.0	580	-	[83]

5.2. M_{SAC}-N-C Catalysts Applied for Zn-Air Batteries

With unique geometric and electronic structures, M_{SAC}-N-C can effectively catalyze the sluggish ORR in metal-air batteries, which help to finish a rapid conversion from chemical energy to electricity. The performance of Zn-air batteries with ZIF-8 derived M_{SAC}-N-C catalysts applied as the air cathode are introduced and compared as follows.

By coating a surfactant of F127 on the Co-N-C, He et al. increased the active center density of Co atoms, thus achieving better electrocatalytic performance [56]. The Co-N-

C@F_{127} catalyst had a half-wave potential ($E_{1/2}$) of 0.84 V in the acidic electrolyte (compared to reversible hydrogen electrode (RHE)), and exhibited excellent stability in corrosive acidic media. It also demonstrated high initial performance with a power density of 0.826 W cm^{-2} along with encouraging durability in Zn-air batteries. A molecular-confined strategy was developed for the synthesis of sub-nano Fe/N/C catalyst pyrolyzed from the $[Fe(CN)_6]^{3-}$@ZIF-8 precursor, through which the individual $[Fe(CN)_6]^{3-}$ ion could be encapsulated into ZIF-8 crystal [92]. The synthesized sub-nano Fe/N/C-20-900 with high BET surface area, appropriate graphitization degree and abundant active sites, exhibited good ORR activity, excellent long-term stability and superb tolerance to methanol. When utilized in Zn-air batteries as the cathode, the sub-nano Fe/N/C-20-900 showed a high open circuit voltage (1.34 V) and high peak power density (22.2 mW cm^{-2}), as well as excellent cycling stability, showing a good application prospect of the sub-nano Fe/N/C-20-900 as the air cathode. Chen et al. fabricated a catalyst comprised of single iron atomic sites supported on a nitrogen, phosphorus and sulfur co-doped hollow carbon polyhedron from a metal-organic framework@polymer composite, which showed promise for substitution of expensive platinum to drive the cathodic oxygen reduction reaction in zinc-air batteries [93]. The maximum power density of Fe-SAs/NPS-HC-based battery achieved as high as 195.0 mW cm^{-2} with a high current density of 375 mA cm^{-2}. Both power density and current density of Fe-SAs/NPS-HC-based battery outperformed that of Pt/C-based battery (177.7 mW cm^{-2}, 283 mA cm^{-2}). Yang et al. reported a copper centered Cu-ISAS/C-N catalyst with an $E_{1/2}$ of 0.92 V in the alkaline electrolyte [79], employed into a primary Zn air battery. The Zn air battery with Cu ISAS/NC catalyst displayed high performance with the maximum power density of up to 280 mW cm^{-2}, superior to Pt/C-based Zn-air battery (200 mW cm^{-2}). At the discharge of 50 mA cm^{-2}, the specific capacity of the Zn-air battery with Cu ISAS/NC catalyst as air-cathode was estimated to be ~736 mAh g^{-1}. More importantly, the Cu ISAS/NC-based battery could robustly serve over 45 h with only a negligible drop of discharge voltage, indicating the excellent stability of the Cu ISAS/NC catalyst in practical Zn-air device. Jin et al. annealed and subsequently mixed ZIF-8 with melamine and transition metal salt to finally synthesize Cu-atoms modified N-doped carbon (NC) catalysts, which exhibited excellent oxygen reduction reaction activity and kinetic performance in alkaline solution [94]. The constructed rechargeable Zn-air battery with Cu-NC and benchmark Pt/C catalyst supported on carbon fiber paper as the cathode and anode, respectively, exhibited high power density (104.5 mW cm^{-2}) at 0.65 V and super good long-term stability with remaining voltaic efficiency of 56% at a charge/discharge current density of 5 mA cm^{-2} after running 250 cycles (ca. 42 h). Wang et al. achieved a Mo-based Mo-N-C_2 catalyst by using a cage-controlled pyrolysis route [74]. In the Mo-N-C_2 catalyst, the Mo has the size ranging from isolated single Mo atom to subnanometer clusters (less than 1 nm). The EXAFS analysis combined with theoretical calculation demonstrated that the local coordination environment of Mo in Mo-N-C_2 catalyst could promote both the ORR and OER performance. When the Mo SACs/N-C was applied as the air electrode for a ZAB assembled, its discharging voltages over a large range of current densities from 10 to 100 mA cm^{-2} were similar to those of the Pt/C-RuO_2 benchmark, and it delivered a high power density of 78 mW cm^{-2}, approaching 70% of that for Pt/C-RuO_2 (112 mW cm^{-2}). Wang et al. successfully synthesized a p-block antimony single-atom catalyst (Sb SAC) with the Sb-N_4 configuration for efficient catalysis of the oxygen reduction reaction (ORR) [95]. The obtained Sb SAC exhibited superior ORR activity with a half-wave potential of 0.86 V and excellent stability, which outperformed most transition-metal (TM, d-block) based SACs and commercial Pt/C. When Sb SAC was employed as the air cathode catalyst to assemble the Zn–air battery, the Sb SAC presented an excellent power density of 184.6 mW cm^{-2} and a high specific capacity (803.5 mAh g^{-1}) in Zn–air battery, achieving about approximately 98.0% utilization of Zn, which outperformed that of commercial Pt/C (96.9% utilization).

The M_{SAC}-N-C catalysts with diatomic catalytic centers are considered to further enhance the ORR activity by the synergistic effect of different TMs. According to the d-band electron model, the molecular interaction between the adsorbents and metal surface obviously relates to the d-band center shift [96]. By introducing heteronuclear TM atoms with different d-band configurations, the electronic structure of the catalyst can be adjusted easily. Among variety of diatomic catalysts, iron-based catalysts with iron and another TM element as co-active centers have attracted the most attention due to the high catalytic activity of Fe-based M_{SAC}-N-C catalysts [97]. Dual-metal-site M_{SAC}-N-C have also been fabricated as the cathode catalysts of fuel cells, where a synergistic effect of double metal sites can lead to excellent catalytic activity and stability.

Gong et al. designed an Fe,Mn-N/C catalyst with Fe and Mn as the diatomic catalytic centers [84]. Their XANES and DFT calculation results demonstrated that the introduction of Mn ions can adjust the electronic structure of Fe ions in the active center of Fe-N_x, and the synergistic interaction between Fe and Mn ions could further reduce the oxygen reduction energy barrier in the ORR process. The catalyst coated carbon paper severed as air-cathode and polished Zn-foil as anode in a home-made Zn-air battery, which showed an open-circuit voltage of 1.45 V and maximal power density of 140 mW cm^{-2}. Zhu et al. innovatively used the template method combined with ion impregnation method to anchor the single Fe and Ni atoms onto the carbon carriers with highly ordered macropores [83]. The Fe and Ni atoms are coordinated in the form of Fe-N_4 and Ni-N_4, respectively, in the prepared Fe/Ni-N_x/OC catalyst. When used in zinc-air batteries, the Fe/Ni-N_x/OC catalyst could exhibit excellent catalytic activity and stability. The Zn air battery with Fe/Ni-N_x/OC-based air cathode could achieve a high open-circuit voltage of 1.525 V and a peak power density of 148 mW cm^{-2} at 210 mA cm^{-2}. Under a high current density of 50 mA cm^{-2}, the Fe/Ni-N_x/OC-based Zn air battery could generate a specific capacity of 712 mAh g^{-1}. An insignificant voltage loss from 0.98 to 1.07 V after 300 successive charge/discharge cycles under a current density of 20 mA cm^{-2} demonstrated a superior cycle performance of Fe/Ni-N_x/OC-based cathode. By introducing Fe^{2+} and Cu^{2+} in the synthesis process of ZIF-8, Wang et al. prepared a Cu@Fe-N-C diatomic catalyst. The obtained Cu@Fe-N-C with many advantages of bimetallic active centers, large specific surface area, high nitrogen doping level and good electrical conductivity, exhibited better ORR performance than that of the Pt/C catalyst in alkaline electrolyte, and similar performance in acidic medium [79]. A home-made zinc air battery was constructed using the Cu@Fe-N-C electrocatalyst dispersed on the hydro-phobic carbon paper as the air cathode. The Cu@Fe-N-C based zinc air battery had an open-circuit voltage of 1.48 V, and assembled from Cu@Fe-N-C owned a peak power density of 92 mW cm^{-2}. When being galvanostatically discharged at a current density of 2 and 20 mA cm^{-2} for 50,000 s, only a small activity loss was observed, which showed that the Cu@Fe-N-C based zinc air batteries were also durable.

In order to directly compare the performance of Zn-air batteries with recently reported M_{SAC}-N-C catalysts derived from M-ZIF-8 precursors, some typical M_{SAC}-N-C catalysts are summarized in Table 2.

Table 2. The performance of Zn-air batteries with recently reported M_{SAC}-N-C catalysts derived from ZIF-8.

Samples	Catalyst Loading Density [mg cm^{-2}]	Peak Power Density (mW cm^{-2})	Durability (h)	Ref.
Co-N-C@C_{F127}	4	826	100	[56]
Fe/N/C-20-900	0.5	22.2	10	[92]
Fe-SAs/NPS-HC	0.8	195	55.56	[93]
Cu-ISAS/C-N	1	280	45	[79]
Cu-NC	0.21	104.5	~42	[94]
Mo SACs/N-C	-	78	120	[74]
Sb SAC	-	184.6	-	[95]
Fe, Mn-N/C-900	1.5	140	6.4	[84]
FeNi0.25-NC	0.255	180	8	[86]
Fe/Ni-N_x/OC	1	148	more than 300	[83]
Cu@Fe-N-C	1	92	~14	[80]

6. Conclusions and Prospects

6.1. Conclusions

This review focuses the main challenges of ZIF-8 derived M_{SAC}-N-C catalysts, and provides an overview of their latest development. In particular, the coordination environments of TM single atoms are very important for the catalytic activity of M_{SAC}-N-C catalysts. Although M_{SAC}-N_4 coordination is the most stable in thermodynamics, research is increasingly proving that the asymmetric coordination environments are conducive to reducing the reaction activation energy barrier of the rate-limiting step of ORR. In addition, although it is generally believed that single atomic catalysts possess much higher catalysis efficiency than that of the metal clusters and nanoparticles, the synergistic effect of metal nanoclusters or nanoparticles and single atom can significantly promote the ORR catalytic activity of M_{SAC}-N-C catalysts. This discovery greatly expands the loadable density of active TM atoms. Furthermore, some typical advanced M_{SAC}-N-C catalysts tested in the fuel cells and zinc-air batteries are comparatively summarized, allowing us to understand intuitively the feasibility of M_{SAC}-N-C catalysts in the future electrochemical conversion and storage devices.

6.2. Prospects

Although researchers have achieved significant progress regarding the M_{SAC}-N-C catalysts derived from ZIF-8, from the practical view, some challenges still need to be taken seriously. (i) The coordination environment has a great influence on the catalytic performance of TM active sites. Therefore, the evolution mechanism from the M-ZIF-8 precursors with ligands and additives to the M_{SAC}-N-C catalysts is worthy of fundamental investigation. More relative information such as molecular structure decomposition and chemical bonding formation should be made available in future studies. (ii) By optimizing the coordination environments and synergistic effect of TMs loading, newer M_{SAC}-N-C catalysts with good activity are expected to develop. (iii) We note that some M_{SAC}-N-C catalysts with similar catalysis performance in RDE measurement system may be greatly different in full cell systems. In fact, the performance of devices is not only related to the M_{SAC}-N-C catalytic performance, but also concerns the device structure and both electrode systems. Therefore, it is key to reasonably optimize the device structure and electrode system to ensure the full use of advanced M_{SAC}-N-C catalysts in full cell devices. In the future, the M_{SAC}-N-C catalysts with high ORR performance are expected to be achieved by lower cost precursors and high efficiency routes.

Author Contributions: Conceptualization, T.Y. and S.Z.; formal analysis, S.S.; investigation, Y.S.; resources, Y.P. and S.X.; data summary, H.S.; writing—original draft preparation, S.S.; writing—review and editing, T.Y. and S.Z.; funding acquisition, T.C. All authors have read and agreed to the published version of the manuscript.

Funding: This research was funded by the National Science Foundation of China [52171218, 21905174 and 51902301], Program of Shanghai Subject Chief Scientist [17XD1403000], the Innovation Program of Shanghai Municipal Education Commission [2019-01-07-00-07-E00015], Shanghai Pujiang Program [21PJ1411100], Shanghai Rising-Star Program [20QA1407100, 21QA1406500], General Program of Natural Science Foundation of Shanghai [20ZR1438400, 22ZR1443900].

Acknowledgments: We acknowledge the support of the National Science Foundation of China (52171218, 21905174 and 51902301). We also acknowledge the support of the Program of Shanghai Subject Chief Scientist (17XD1403000), the Innovation Program of Shanghai Municipal Education Commission (2019-01-07-00-07-E00015), Shanghai Pujiang Program (21PJ1411100), Shanghai Rising-Star Program (20QA1407100, 21QA1406500), General Program of Natural Science Foundation of Shanghai (20ZR1438400, 22ZR1443900).

Conflicts of Interest: The authors declare no conflict of interest.

References

1. Zhang, C.; Huang, K. A Comprehensive Review on the Development of Solid-State Metal-Air Batteries Operated on Oxide-Ion Chemistry. *Adv. Energy Mater.* **2020**, *11*, 2000630. [CrossRef]
2. Liu, Y.; Shao, Z.; Mori, T.; Jiang, S.P. Development of nickel based cermet anode materials in solid oxide fuel cells-Now and future. *Mater. Rep. Energy* **2021**, *1*, 100003. [CrossRef]
3. Sun, T.; Zhao, S.; Chen, W.; Zhai, D.; Dong, J.; Wang, Y.; Zhang, S.; Han, A.; Gu, L.; Yu, R.; et al. Single-atomic cobalt sites embedded in hierarchically ordered porous nitrogen-doped carbon as a superior bifunctional electrocatalyst. *Proc. Natl. Acad. Sci. USA* **2018**, *115*, 12692–12697. [CrossRef] [PubMed]
4. Wang, D.; Min, Y.; Yu, Y.; Peng, B. A general approach for fabrication of nitrogen-doped graphene sheets and its application in supercapacitors. *J. Colloid Interf. Sci.* **2014**, *417*, 270–277. [CrossRef]
5. Li, M.; Bi, X.; Wang, R.; Li, Y.; Jiang, G.; Li, L.; Zhong, C.; Chen, Z.; Lu, J. Relating Catalysis between Fuel Cell and Metal-Air Batteries. *Matter* **2020**, *2*, 32–49. [CrossRef]
6. Bai, P.; Viswanathan, V.; Bazant, M.Z. A dual-mode rechargeable lithium–bromine/oxygen fuel cell. *J. Mater. Chem. A* **2015**, *3*, 14165–14172. [CrossRef]
7. Yang, L.; Shi, L.; Wang, D.; Lv, Y.; Cao, D. Single-atom cobalt electrocatalysts for foldable solid-state Zn-air battery. *Nano Energy* **2018**, *50*, 691–698. [CrossRef]
8. Zhang, L.; Shao, Q.; Zhang, J. An overview of non-noble metal electrocatalysts and their associated air cathodes for Mg-air batteries. *Mater. Rep. Energy* **2021**, *1*, 100002. [CrossRef]
9. Zeng, S.; Tong, X.; Zhou, S.; Lv, B.; Qiao, J.; Song, Y.; Chen, M.; Di, J.; Li, Q. All-in-One Bifunctional Oxygen Electrode Films for Flexible Zn-Air Batteries. *Small* **2018**, *14*, 1803409. [CrossRef]
10. Zhu, C.; Yin, Z.; Lai, W.; Sun, Y.; Liu, L.; Zhang, X.; Chen, Y.; Chou, S.-L. Fe-Ni-Mo Nitride Porous Nanotubes for Full Water Splitting and Zn-Air Batteries. *Adv. Energy Mater.* **2018**, *8*, 1802327. [CrossRef]
11. Zaman, S.; Huang, L.; Douka, A.I.; Yang, H.; You, B.; Xia, B.Y. Oxygen Reduction Electrocatalysts toward Practical Fuel Cells: Progress and Perspectives. *Angew. Chem. Int. Ed.* **2021**, *60*, 17832–17852. [CrossRef] [PubMed]
12. Shao, M.; Chang, Q.; Dodelet, J.P.; Chenitz, R. Recent Advances in Electrocatalysts for Oxygen Reduction Reaction. *Chem. Rev.* **2016**, *116*, 3594–3657. [CrossRef] [PubMed]
13. Peng, Z.; Yang, H. Designer platinum nanoparticles: Control of shape, composition in alloy, nanostructure and electrocatalytic property. *Nano Today* **2009**, *4*, 143–164. [CrossRef]
14. Gao, P.; Pu, M.; Chen, Q.; Zhu, H. Pt-Based Intermetallic Nanocrystals in Cathode Catalysts for Proton Exchange Membrane Fuel Cells: From Precise Synthesis to Oxygen Reduction Reaction Strategy. *Catalysts* **2021**, *11*, 1050. [CrossRef]
15. Nie, Y.; Li, L.; Wei, Z. Recent advancements in Pt and Pt-free catalysts for oxygen reduction reaction. *Chem. Soc. Rev.* **2015**, *44*, 2168–2201. [CrossRef]
16. Sun, K.; Cheng, T.; Wu, L.; Hu, Y.; Zhou, J.; Maclennan, A.; Jiang, Z.; Gao, Y.; Goddard, W.A., 3rd; Wang, Z. Ultrahigh Mass Activity for Carbon Dioxide Reduction Enabled by Gold-Iron Core-Shell Nanoparticles. *J. Am. Chem. Soc.* **2017**, *139*, 15608–15611. [CrossRef]
17. Lu, C.; Tranca, D.; Zhang, J.; Rodri Guez Hernandez, F.N.; Su, Y.; Zhuang, X.; Zhang, F.; Seifert, G.; Feng, X. Molybdenum Carbide-Embedded Nitrogen-Doped Porous Carbon Nanosheets as Electrocatalysts for Water Splitting in Alkaline Media. *ACS Nano* **2017**, *11*, 3933–3942. [CrossRef]
18. He, C.; Ma, Z.; Wu, Q.; Cai, Y.; Huang, Y.; Liu, K.; Fan, Y.; Wang, H.; Li, Q.; Qi, J.; et al. Promoting the ORR catalysis of Pt-Fe intermetallic catalysts by increasing atomic utilization and electronic regulation. *Electrochim. Acta* **2020**, *330*, 135119. [CrossRef]
19. Wang, Y.-J.; Fang, B.; Li, H.; Bi, X.T.; Wang, H. Progress in modified carbon support materials for Pt and Pt-alloy cathode catalysts in polymer electrolyte membrane fuel cells. *Prog. Mater. Sci.* **2016**, *82*, 445–498. [CrossRef]
20. Ioroi, T.; Siroma, Z.; Yamazaki, S.I.; Yasuda, K. Electrocatalysts for PEM Fuel Cells. *Adv. Energy Mater.* **2019**, *9*, 1801284. [CrossRef]
21. Zhang, H.; An, P.; Zhou, W.; Guan, B.Y.; Zhang, P.; Dong, J.; Lou, X.W.D. Dynamic traction of lattice-confined platinum atoms into mesoporous carbon matrix for hydrogen evolution reaction. *Sci. Adv.* **2018**, *4*, eaao6657. [CrossRef] [PubMed]
22. Tian, X.L.; Xu, Y.Y.; Zhang, W.; Wu, T.; Xia, B.Y.; Wang, X. Unsupported Platinum-Based Electrocatalysts for Oxygen Reduction Reaction. *ACS Energy Lett.* **2017**, *2*, 2035–2043. [CrossRef]
23. Gao, X.; He, L.; Yu, H.; Xie, F.; Yang, Y.; Shao, Z. The non-precious metal ORR catalysts for the anion exchange membrane fuel cells application: A numerical simulation and experimental study. *Int. J. Hydrogen Energy* **2020**, *45*, 23353–23367. [CrossRef]
24. Kumar, K.; Canaff, C.; Rousseau, J.; Arrii-Clacens, S.; Napporn, T.W.; Habrioux, A.; Kokoh, K.B. Effect of the Oxide–Carbon Heterointerface on the Activity of Co_3O_4/NRGO Nanocomposites toward ORR and OER. *J. Phys. Chem. C* **2016**, *120*, 7949–7958. [CrossRef]
25. Hong, Q.; Lu, H.; Cao, Y. Improved oxygen reduction activity and stability on N, S-enriched hierarchical carbon architectures with decorating core-shell iron group metal sulphides nanoparticles for Al-air batteries. *Carbon* **2019**, *145*, 53–60. [CrossRef]
26. Cui, L.; Cui, L.; Li, Z.; Zhang, J.; Wang, H.; Lu, S.; Xiang, Y. A copper single-atom catalyst towards efficient and durable oxygen reduction for fuel cells. *J. Mater. Chem. A* **2019**, *7*, 16690–16695. [CrossRef]
27. Yu, J.; Dai, Y.; He, Q.; Zhao, D.; Shao, Z.; Ni, M. A mini-review of noble-metal-free electrocatalysts for overall water splitting in non-alkaline electrolytes. *Mater. Rep. Energy* **2021**, *1*, 100024. [CrossRef]

28. Liu, X.; Chen, C.; Cheng, Q.; Zou, L.; Zou, Z.; Yang, H. Binary Nitrogen Precursor-Derived Porous Fe-N-S/C Catalyst for Efficient Oxygen Reduction Reaction in a Zn-Air Battery. *Catalysts* **2018**, *8*, 158. [CrossRef]
29. Singh, H.; Zhuang, S.; Nunna, B.; Lee, E. Thermal Stability and Potential Cycling Durability of Nitrogen-Doped Graphene Modified by Metal-Organic Framework for Oxygen Reduction Reactions. *Catalysts* **2018**, *8*, 607. [CrossRef]
30. Han, A.; Wang, B.; Kumar, A.; Qin, Y.; Jin, J.; Wang, X.; Yang, C.; Dong, B.; Jia, Y.; Liu, J.; et al. Recent Advances for MOF-Derived Carbon-Supported Single-Atom Catalysts. *Small Methods* **2019**, *3*, 1800471. [CrossRef]
31. Su, C.; Liu, Y.; Luo, Z.; Veder, J.-P.; Zhong, Y.; Jiang, S.P.; Shao, Z. Defects-rich porous carbon microspheres as green electrocatalysts for efficient and stable oxygen-reduction reaction over a wide range of pH values. *Chem. Eng. J.* **2021**, *406*, 126883. [CrossRef]
32. Li, J.; Zhang, H.; Samarakoon, W.; Shan, W.; Cullen, D.A.; Karakalos, S.; Chen, M.; Gu, D.; More, K.L.; Wang, G.; et al. Thermally Driven Structure and Performance Evolution of Atomically Dispersed FeN_4 Sites for Oxygen Reduction. *Angew. Chem. Int. Ed.* **2019**, *58*, 18971–18980. [CrossRef] [PubMed]
33. Zhang, X.; Guo, J.; Guan, P.; Liu, C.; Huang, H.; Xue, F.; Dong, X.; Pennycook, S.J.; Chisholm, M.F. Catalytically active single-atom niobium in graphitic layers. *Nat. Commun.* **2013**, *4*, 1924. [CrossRef] [PubMed]
34. Liang, Z.; Qu, C.; Xia, D.; Zou, R.; Xu, Q. Atomically Dispersed Metal Sites in MOF-Based Materials for Electrocatalytic and Photocatalytic Energy Conversion. *Angew. Chem. Int. Ed.* **2018**, *57*, 9604–9633. [CrossRef] [PubMed]
35. Lu, X.F.; Xia, B.Y.; Zang, S.Q.; Lou, X.W.D. Metal-Organic Frameworks Based Electrocatalysts for the Oxygen Reduction Reaction. *Angew. Chem. Int. Ed.* **2020**, *59*, 4634–4650. [CrossRef] [PubMed]
36. Chen, L.; Liu, X.; Zheng, L.; Li, Y.; Guo, X.; Wan, X.; Liu, Q.; Shang, J.; Shui, J. Insights into the role of active site density in the fuel cell performance of Co-N-C catalysts. *Appl. Catal. B Environ.* **2019**, *256*, 117849. [CrossRef]
37. Wang, B.; Tang, J.; Zhang, X.; Hong, M.; Yang, H.; Guo, X.; Xue, S.; Du, C.; Liu, Z.; Chen, J. Nitrogen doped porous carbon polyhedral supported Fe and Ni dual-metal single-atomic catalysts: Template-free and metal ligand-free sysnthesis with microwave-assistance and d-band center modulating for boosted ORR catalysis in zinc-air batteries. *Chem. Eng. J.* **2022**, *437*, 135295. [CrossRef]
38. Zhang, S.; Xue, H.; Li, W.L.; Sun, J.; Guo, N.; Song, T.; Dong, H.; Zhang, J.; Ge, X.; Zhang, W.; et al. Constructing Precise Coordination of Nickel Active Sites on Hierarchical Porous Carbon Framework for Superior Oxygen Reduction. *Small* **2021**, *17*, 2102125. [CrossRef]
39. Fan, M.; Cui, J.; Zhang, J.; Wu, J.; Chen, S.; Song, L.; Wang, Z.; Wang, A.; Vajtai, R.; Wu, Y.; et al. The modulating effect of N coordination on single-atom catalysts researched by Pt-N-C model through both experimental study and DFT simulation. *J. Mater. Sci. Technol.* **2021**, *91*, 160–167. [CrossRef]
40. Ma, S.; Han, Z.; Leng, K.; Liu, X.; Wang, Y.; Qu, Y.; Bai, J. Ionic Exchange of Metal-Organic Frameworks for Constructing Unsaturated Copper Single-Atom Catalysts for Boosting Oxygen Reduction Reaction. *Small* **2020**, *16*, 2001384. [CrossRef]
41. Lai, Q.; Zheng, L.; Liang, Y.; He, J.; Zhao, J.; Chen, J. Metal–Organic-Framework-Derived Fe-N/C Electrocatalyst with Five-Coordinated Fe-N_x Sites for Advanced Oxygen Reduction in Acid Media. *ACS Catal.* **2017**, *7*, 1655–1663. [CrossRef]
42. Ye, W.; Chen, S.; Lin, Y.; Yang, L.; Chen, S.; Zheng, X.; Qi, Z.; Wang, C.; Long, R.; Chen, M.; et al. Precisely Tuning the Number of Fe Atoms in Clusters on N-Doped Carbon toward Acidic Oxygen Reduction Reaction. *Chem* **2019**, *5*, 2865–2878. [CrossRef]
43. Liu, X.; Liu, H.; Chen, C.; Zou, L.; Li, Y.; Zhang, Q.; Yang, B.; Zou, Z.; Yang, H. Fe_2N nanoparticles boosting FeN_x moieties for highly efficient oxygen reduction reaction in Fe-N-C porous catalyst. *Nano Res.* **2019**, *12*, 1651–1657. [CrossRef]
44. Chen, M.; He, Y.; Spendelow, J.S.; Wu, G. Atomically Dispersed Metal Catalysts for Oxygen Reduction. *ACS Energy Lett.* **2019**, *4*, 1619–1633. [CrossRef]
45. Li, Z.; Gao, Q.; Qian, W.; Tian, W.; Zhang, H.; Zhang, Q.; Liu, Z. Ultrahigh Oxygen Reduction Reaction Electrocatalytic Activity and Stability over Hierarchical Nanoporous N-doped Carbon. *Sci. Rep.* **2018**, *8*, 2863. [CrossRef] [PubMed]
46. Cui, N.; Bi, K.; Sun, W.; Wu, Q.; Li, Y.; Xu, T.; Lv, B.; Zhang, S. Effect of Pyrolysis Conditions on the Performance of Co–Doped MOF–Derived Carbon Catalysts for Oxygen Reduction Reaction. *Catalysts* **2021**, *11*, 1163. [CrossRef]
47. Hayashi, H.; Cote, A.P.; Furukawa, H.; O'Keeffe, M.; Yaghi, O.M. Zeolite A imidazolate frameworks. *Nat. Mater.* **2007**, *6*, 501–506. [CrossRef] [PubMed]
48. Tian, Y.Q.; Zhao, Y.M.; Chen, Z.X.; Zhang, G.N.; Weng, L.H.; Zhao, D.Y. Design and generation of extended zeolitic metal-organic frameworks (ZMOFs): Synthesis and crystal structures of zinc(II) imidazolate polymers with zeolitic topologies. *Chem. Eur. J.* **2007**, *13*, 4146–4154. [CrossRef] [PubMed]
49. Venna, S.R.; Jasinski, J.B.; Carreon, M.A. Structural Evolution of Zeolitic Imidazolate Framework-8. *J. Am. Chem. Soc.* **2010**, *132*, 18030–18033. [CrossRef] [PubMed]
50. Bustamante, E.L.; Fernandez, J.L.; Zamaro, J.M. Influence of the solvent in the synthesis of zeolitic imidazolate framework-8 (ZIF-8) nanocrystals at room temperature. *J. Colloid Interf. Sci.* **2014**, *424*, 37–43. [CrossRef]
51. Razmjooei, F.; Yu, J.-H.; Lee, H.-Y.; Lee, B.-J.; Singh, K.P.; Kang, T.-H.; Kim, H.-J.; Yu, J.-S. Single-Atom Iron-Based Electrocatalysts for High-Temperature Polymer Electrolyte Membrane Fuel Cell: Organometallic Precursor and Pore Texture Tailoring. *ACS Appl. Energy Mater.* **2020**, *3*, 11164–11176. [CrossRef]
52. Liu, B.; Zhou, H.; Jin, H.; Zhu, J.; Wang, Z.; Hu, C.; Liang, L.; Mu, S.; He, D. A new strategy to access Co/N co-doped carbon nanotubes as oxygen reduction reaction catalysts. *Chin. Chem. Lett.* **2021**, *32*, 535–538. [CrossRef]

53. Chen, Y.; Ji, S.; Wang, Y.; Dong, J.; Chen, W.; Li, Z.; Shen, R.; Zheng, L.; Zhuang, Z.; Wang, D.; et al. Isolated Single Iron Atoms Anchored on N-Doped Porous Carbon as an Efficient Electrocatalyst for the Oxygen Reduction Reaction. *Angew. Chem. Int. Ed.* **2017**, *56*, 6937–6941. [CrossRef]
54. Xiao, M.; Zhu, J.; Ma, L.; Jin, Z.; Ge, J.; Deng, X.; Hou, Y.; He, Q.; Li, J.; Jia, Q.; et al. Microporous Framework Induced Synthesis of Single-Atom Dispersed Fe-N-C Acidic ORR Catalyst and Its in Situ Reduced Fe-N_4 Active Site Identification Revealed by X-ray Absorption Spectroscopy. *ACS Catal.* **2018**, *8*, 2824–2832. [CrossRef]
55. Xu, X.; Zhang, X.; Xia, Z.; Sun, R.; Li, H.; Wang, J.; Yu, S.; Wang, S.; Sun, G. Solid phase microwave-assisted fabrication of Fe-doped ZIF-8 for single-atom Fe-N-C electrocatalysts on oxygen reduction. *J. Energy Chem.* **2021**, *54*, 579–586. [CrossRef]
56. He, Y.; Hwang, S.; Cullen, D.A.; Uddin, M.A.; Langhorst, L.; Li, B.; Karakalos, S.; Kropf, A.J.; Wegener, E.C.; Sokolowski, J.; et al. Highly active atomically dispersed CoN_4 fuel cell cathode catalysts derived from surfactant-assisted MOFs: Carbon-shell confinement strategy. *Energy Environ. Sci.* **2019**, *12*, 250–260. [CrossRef]
57. He, Y.; Shi, Q.; Shan, W.; Li, X.; Kropf, A.J.; Wegener, E.C.; Wright, J.; Karakalos, S.; Su, D.; Cullen, D.A.; et al. Dynamically Unveiling Metal-Nitrogen Coordination during Thermal Activation to Design High-Efficient Atomically Dispersed CoN_4 Active Sites. *Angew. Chem. Int. Ed.* **2021**, *60*, 9516–9526. [CrossRef]
58. Ha, Y.; Fei, B.; Yan, X.; Xu, H.; Chen, Z.; Shi, L.; Fu, M.; Xu, W.; Wu, R. Atomically Dispersed Co-Pyridinic N-C for Superior Oxygen Reduction Reaction. *Adv. Energy Mater.* **2020**, *10*, 2002592. [CrossRef]
59. Im, K.; Jang, J.-H.; Heo, J.; Kim, D.; Lee, K.-S.; Lim, H.-K.; Kim, J.; Yoo, S.J. Design of Co-NC as efficient electrocatalyst: The unique structure and active site for remarkable durability of proton exchange membrane fuel cells. *Appl. Catal. B Environ.* **2022**, *308*, 121220. [CrossRef]
60. Chen, Y.; Gao, R.; Ji, S.; Li, H.; Tang, K.; Jiang, P.; Hu, H.; Zhang, Z.; Hao, H.; Qu, Q.; et al. Atomic-Level Modulation of Electronic Density at Cobalt Single-Atom Sites Derived from Metal-Organic Frameworks: Enhanced Oxygen Reduction Performance. *Angew. Chem. Int. Ed.* **2021**, *60*, 3212–3221. [CrossRef]
61. Song, Z.; Zhu, Y.N.; Liu, H.; Banis, M.N.; Zhang, L.; Li, J.; Doyle-Davis, K.; Li, R.; Sham, T.K.; Yang, L.; et al. Engineering the Low Coordinated Pt Single Atom to Achieve the Superior Electrocatalytic Performance toward Oxygen Reduction. *Small* **2020**, *16*, 2003096. [CrossRef] [PubMed]
62. Wang, X.X.; Cullen, D.A.; Pan, Y.T.; Hwang, S.; Wang, M.; Feng, Z.; Wang, J.; Engelhard, M.H.; Zhang, H.; He, Y.; et al. Nitrogen-Coordinated Single Cobalt Atom Catalysts for Oxygen Reduction in Proton Exchange Membrane Fuel Cells. *Adv. Mater.* **2018**, *30*, 1706758. [CrossRef] [PubMed]
63. Wang, X.; Chen, Z.; Zhao, X.; Yao, T.; Chen, W.; You, R.; Zhao, C.; Wu, G.; Wang, J.; Huang, W.; et al. Regulation of Coordination Number over Single Co Sites: Triggering the Efficient Electroreduction of CO_2. *Angew. Chem. Int. Ed.* **2018**, *57*, 1944–1948. [CrossRef] [PubMed]
64. Yi, J.-D.; Xu, R.; Wu, Q.; Zhang, T.; Zang, K.-T.; Luo, J.; Liang, Y.-L.; Huang, Y.-B.; Cao, R. Atomically Dispersed Iron–Nitrogen Active Sites within Porphyrinic Triazine-Based Frameworks for Oxygen Reduction Reaction in Both Alkaline and Acidic Media. *ACS Energy Lett.* **2018**, *3*, 883–889. [CrossRef]
65. Jiang, R.; Li, L.; Sheng, T.; Hu, G.; Chen, Y.; Wang, L. Edge-Site Engineering of Atomically Dispersed Fe-N_4 by Selective C-N Bond Cleavage for Enhanced Oxygen Reduction Reaction Activities. *J. Am. Chem. Soc.* **2018**, *140*, 11594–11598. [CrossRef]
66. Qu, Y.; Li, Z.; Chen, W.; Lin, Y.; Yuan, T.; Yang, Z.; Zhao, C.; Wang, J.; Zhao, C.; Wang, X.; et al. Direct transformation of bulk copper into copper single sites via emitting and trapping of atoms. *Nat. Catal.* **2018**, *1*, 781–786. [CrossRef]
67. Shang, L.; Yu, H.; Huang, X.; Bian, T.; Shi, R.; Zhao, Y.; Waterhouse, G.I.; Wu, L.Z.; Tung, C.H.; Zhang, T. Well-Dispersed ZIF-Derived Co,N-Co-doped Carbon Nanoframes through Mesoporous-Silica-Protected Calcination as Efficient Oxygen Reduction Electrocatalysts. *Adv. Mater.* **2016**, *28*, 1668–1674. [CrossRef]
68. Zhou, H.; Yang, T.; Kou, Z.; Shen, L.; Zhao, Y.; Wang, Z.; Wang, X.; Yang, Z.; Du, J.; Xu, J.; et al. Negative Pressure Pyrolysis Induced Highly Accessible Single Sites Dispersed on 3D Graphene Frameworks for Enhanced Oxygen Reduction. *Angew. Chem. Int. Ed.* **2020**, *59*, 20465–20469. [CrossRef]
69. Liu, D.; Li, J.C.; Ding, S.; Lyu, Z.; Feng, S.; Tian, H.; Huyan, C.; Xu, M.; Li, T.; Du, D.; et al. 2D Single-Atom Catalyst with Optimized Iron Sites Produced by Thermal Melting of Metal-Organic Frameworks for Oxygen Reduction Reaction. *Small Methods* **2020**, *4*, 1900827. [CrossRef]
70. Han, X.; Ling, X.; Wang, Y.; Ma, T.; Zhong, C.; Hu, W.; Deng, Y. Generation of Nanoparticle, Atomic-Cluster, and Single-Atom Cobalt Catalysts from Zeolitic Imidazole Frameworks by Spatial Isolation and Their Use in Zinc-Air Batteries. *Angew. Chem. Int. Ed.* **2019**, *58*, 5359–5364. [CrossRef]
71. Ao, X.; Zhang, W.; Li, Z.; Li, J.G.; Soule, L.; Huang, X.; Chiang, W.H.; Chen, H.M.; Wang, C.; Liu, M.; et al. Markedly Enhanced Oxygen Reduction Activity of Single-Atom Fe Catalysts via Integration with Fe Nanoclusters. *ACS Nano* **2019**, *13*, 11853–11862. [CrossRef]
72. Kratzl, K.; Kratky, T.; Gunther, S.; Tomanec, O.; Zboril, R.; Michalicka, J.; Macak, J.M.; Cokoja, M.; Fischer, R.A. Generation and Stabilization of Small Platinum Clusters $Pt^{12+}/^{-x}$ Inside a Metal-Organic Framework. *J. Am. Chem. Soc.* **2019**, *141*, 13962–13969. [CrossRef]
73. Zhai, W.; Huang, S.; Lu, C.; Tang, X.; Li, L.; Huang, B.; Hu, T.; Yuan, K.; Zhuang, X.; Chen, Y. Simultaneously Integrate Iron Single Atom and Nanocluster Triggered Tandem Effect for Boosting Oxygen Electroreduction. *Small* **2022**, *18*, 2107225. [CrossRef]

74. Kou, Z.; Zang, W.; Ma, Y.; Pan, Z.; Mu, S.; Gao, X.; Tang, B.; Xiong, M.; Zhao, X.; Cheetham, A.K.; et al. Cage-confinement pyrolysis route to size-controlled molybdenum-based oxygen electrode catalysts: From isolated atoms to clusters and nanoparticles. *Nano Energy* **2020**, *67*, 104288. [CrossRef]
75. Wang, Z.; Zhu, C.; Tan, H.; Liu, J.; Xu, L.; Zhang, Y.; Liu, Y.; Zou, X.; Liu, Z.; Lu, X. Understanding the Synergistic Effects of Cobalt Single Atoms and Small Nanoparticles: Enhancing Oxygen Reduction Reaction Catalytic Activity and Stability for Zinc-Air Batteries. *Adv. Funct. Mater.* **2021**, *31*, 2104735. [CrossRef]
76. Li, J.; Chen, M.; Cullen, D.A.; Hwang, S.; Wang, M.; Li, B.; Liu, K.; Karakalos, S.; Lucero, M.; Zhang, H.; et al. Atomically dispersed manganese catalysts for oxygen reduction in proton-exchange membrane fuel cells. *Nat. Catal.* **2018**, *1*, 935–945. [CrossRef]
77. Luo, E.; Zhang, H.; Wang, X.; Gao, L.; Gong, L.; Zhao, T.; Jin, Z.; Ge, J.; Jiang, Z.; Liu, C.; et al. Single-Atom Cr-N_4 Sites Designed for Durable Oxygen Reduction Catalysis in Acid Media. *Angew. Chem. Int. Ed.* **2019**, *58*, 12469–12475. [CrossRef]
78. Jiang, B.; Sun, H.; Yuan, T.; He, W.; Zheng, C.; Zhang, H.-J.; Yang, J.; Zheng, S. Framework-Derived Tungsten Single-Atom Catalyst for Oxygen Reduction Reaction. *Energy Fuel* **2021**, *35*, 8173–8180. [CrossRef]
79. Yang, Z.; Chen, B.; Chen, W.; Qu, Y.; Zhou, F.; Zhao, C.; Xu, Q.; Zhang, Q.; Duan, X.; Wu, Y. Directly transforming copper (I) oxide bulk into isolated single-atom copper sites catalyst through gas-transport approach. *Nat. Commun.* **2019**, *10*, 3734. [CrossRef]
80. Wang, Z.; Jin, H.; Meng, T.; Liao, K.; Meng, W.; Yang, J.; He, D.; Xiong, Y.; Mu, S. Fe, Cu-Coordinated ZIF-Derived Carbon Framework for Efficient Oxygen Reduction Reaction and Zinc-Air Batteries. *Adv. Funct. Mater.* **2018**, *28*, 1802596. [CrossRef]
81. Wang, J.; Huang, Z.; Liu, W.; Chang, C.; Tang, H.; Li, Z.; Chen, W.; Jia, C.; Yao, T.; Wei, S.; et al. Design of N-Coordinated Dual-Metal Sites: A Stable and Active Pt-Free Catalyst for Acidic Oxygen Reduction Reaction. *J. Am. Chem. Soc.* **2017**, *139*, 17281–17284. [CrossRef]
82. Zhang, D.; Chen, W.; Li, Z.; Chen, Y.; Zheng, L.; Gong, Y.; Li, Q.; Shen, R.; Han, Y.; Cheong, W.C.; et al. Isolated Fe and Co dual active sites on nitrogen-doped carbon for a highly efficient oxygen reduction reaction. *Chem. Commun.* **2018**, *54*, 4274–4277. [CrossRef]
83. Zhu, Z.; Yin, H.; Wang, Y.; Chuang, C.H.; Xing, L.; Dong, M.; Lu, Y.R.; Casillas-Garcia, G.; Zheng, Y.; Chen, S.; et al. Coexisting Single-Atomic Fe and Ni Sites on Hierarchically Ordered Porous Carbon as a Highly Efficient ORR Electrocatalyst. *Adv. Mater.* **2020**, *32*, 2004670. [CrossRef]
84. Gong, S.; Wang, C.; Jiang, P.; Hu, L.; Lei, H.; Chen, Q. Designing highly efficient dual-metal single-atom electrocatalysts for the oxygen reduction reaction inspired by biological enzyme systems. *J. Mater. Chem. A* **2018**, *6*, 13254–13262. [CrossRef]
85. Liu, F.; Shi, L.; Lin, X.; Yu, D.; Zhang, C.; Xu, R.; Liu, D.; Qiu, J.; Dai, L. Site-density engineering of single-atomic iron catalysts for high-performance proton exchange membrane fuel cells. *Appl. Catal. B Environ.* **2022**, *302*, 120860. [CrossRef]
86. Liu, J.; Fan, C.; Liu, G.; Jiang, L. MOF-derived dual metal (Fe, Ni)-nitrogen–doped carbon for synergistically enhanced oxygen reduction reaction. *Appl. Surf. Sci.* **2021**, *538*, 148017. [CrossRef]
87. Xu, J.; Liang, G.; Chen, D.; Li, Z.; Zhang, H.; Chen, J.; Xie, F.; Jin, Y.; Wang, N.; Meng, H. Iron and nitrogen doped carbon derived from ferrocene and ZIF-8 as proton exchange membrane fuel cell cathode catalyst. *Appl. Surf. Sci.* **2022**, *573*, 151607. [CrossRef]
88. Qiao, M.; Wang, Y.; Wang, Q.; Hu, G.; Mamat, X.; Zhang, S.; Wang, S. Hierarchically Ordered Porous Carbon with Atomically Dispersed FeN_4 for Ultraefficient Oxygen Reduction Reaction in Proton-Exchange Membrane Fuel Cells. *Angew. Chem. Int. Ed.* **2020**, *59*, 2688–2694. [CrossRef]
89. Deng, Y.; Chi, B.; Tian, X.; Cui, Z.; Liu, E.; Jia, Q.; Fan, W.; Wang, G.; Dang, D.; Li, M.; et al. g-C_3N_4 promoted MOF derived hollow carbon nanopolyhedra doped with high density/fraction of single Fe atoms as an ultra-high performance non-precious catalyst towards acidic ORR and PEM fuel cells. *J. Mater. Chem. A* **2019**, *7*, 5020–5030. [CrossRef]
90. Chen, M.; Li, X.; Yang, F.; Li, B.; Stracensky, T.; Karakalos, S.; Mukerjee, S.; Jia, Q.; Su, D.; Wang, G.; et al. Atomically Dispersed MnN_4 Catalysts via Environmentally Benign Aqueous Synthesis for Oxygen Reduction: Mechanistic Understanding of Activity and Stability Improvements. *ACS Catal.* **2020**, *10*, 10523–10534. [CrossRef]
91. Zhao, H.; Qian, L.; Chen, Y.; Wang, Q.; Zhao, G. Selective catalytic two-electron O_2 reduction for onsite efficient oxidation reaction in heterogeneous electro-Fenton process. *Chem. Eng. J.* **2018**, *332*, 486–498. [CrossRef]
92. Chen, D.; Ji, J.; Jiang, Z.; Ling, M.; Jiang, Z.; Peng, X. Molecular-confinement synthesis of sub-nano Fe/N/C catalysts with high oxygen reduction reaction activity and excellent durability for rechargeable Zn-Air batteries. *J. Power Sources* **2020**, *450*, 227660. [CrossRef]
93. Chen, Y.; Ji, S.; Zhao, S.; Chen, W.; Dong, J.; Cheong, W.C.; Shen, R.; Wen, X.; Zheng, L.; Rykov, A.I.; et al. Enhanced oxygen reduction with single-atomic-site iron catalysts for a zinc-air battery and hydrogen-air fuel cell. *Nat. Commun.* **2018**, *9*, 5422. [CrossRef]
94. Jin, W.; Lu, Z.; Wang, Q.; Zhu, Y.; Pan, H.; Yao, S.; Fang, Z.; Huang, X.; Chen, X. Atomic Cu dispersed ZIF-8 derived N-doped carbon for high-performance oxygen electrocatalysis in Zn-air battery. *J. Phys. Mater.* **2021**, *4*, 024006. [CrossRef]
95. Wang, T.; Cao, X.; Qin, H.; Shang, L.; Zheng, S.; Fang, F.; Jiao, L. P-Block Atomically Dispersed Antimony Catalyst for Highly Efficient Oxygen Reduction Reaction. *Angew. Chem. Int. Ed.* **2021**, *60*, 21237–21241. [CrossRef]
96. Bai, L.; Hsu, C.S.; Alexander, D.T.L.; Chen, H.M.; Hu, X. A Cobalt-Iron Double-Atom Catalyst for the Oxygen Evolution Reaction. *J. Am. Chem. Soc.* **2019**, *141*, 14190–14199. [CrossRef]
97. Wang, J.; Liu, W.; Luo, G.; Li, Z.; Zhao, C.; Zhang, H.; Zhu, M.; Xu, Q.; Wang, X.; Zhao, C.; et al. Synergistic effect of well-defined dual sites boosting the oxygen reduction reaction. *Energy Environ. Sci.* **2018**, *11*, 3375–3379. [CrossRef]